

Application of a critical state model to the Merriespruit tailings dam failure

Miguel A. Mánica^{*1}, Marcos Arroyo², Antonio Gens², and Lluís Monforte³

¹Institute of Engineering, National Autonomous University of Mexico, Mexico City, Mexico.

²Department of Civil and Environmental Engineering, Universitat Politècnica de Catalunya, Barcelona Tech - CIMNE, Barcelona, Spain.

³CIMNE, International Centre for Numerical Methods in Engineering, Barcelona, Spain.

Abstract

The use of stress-deformation analyses to evaluate the characteristics of possible static liquefaction events is rapidly becoming the norm for tailings dams exposed to such risk. Ideally, those analyses should be based on constitutive models that incorporate the fundamental mechanics of the problem, that are able to perform robustly in commercial numerical platforms, and are simple to calibrate. This work proposes a model that aims to fulfil that specification. The model presented is a new implementation of CASM (Clay And Sand Model), a model based on critical state concepts able to represent static liquefaction. The model formulation is elaborated to show that all required inputs can be related to familiar concepts such as the critical state line, the state parameter, the normalised undrained peak strength, or the coefficient of earth pressure at rest. The methodology is then illustrated by analysing the failure of the Merriespruit tailings dam, which took place in South Africa in 1994 and was instrumental in the recognition of how widespread liquefaction risk might be in saturated tailings. Numerical analysis of the case evidences how a large static liquefaction failure might have been triggered by a relatively small slope erosion caused by overtopping.

1 Introduction

Current worldwide estimates (Franks et al., 2020) indicate that there are over 3000 active tailings facilities in the world and a larger number of inactive or closed ones. Driven by decreasing ore grades and strong demand (Giurco et al., 2019), the need for such facilities is likely to increase in the future. Unfortunately, the safety track record of tailing facilities is significantly below that of comparable geotechnical structures such as water dams (Davies et al., 2001; Morgenstern, 2018), and failures involving large consequences are too frequent. This has prompted

^{*}Corresponding author: mmanicam@iingen.unam.mx

large collective efforts aiming to improve this situation (ICMM et al., 2020). Geotechnical engineering can contribute by developing tools that allow a realistic evaluation of dam safety against critical failure modes.

Static liquefaction of tailings has been repeatedly identified as the most important contributing factor in major incidents (Davies, 2002; Been, 2016; Morgenstern, 2018), including, in the last decade, those at Fundão (Morgenstern et al., 2015) and Brumadinho (Robertson et al., 2019). Even when the root cause is found elsewhere (e.g. at a weak foundation layer), static liquefaction of tailings does much to aggravate the failure, as seen in the cases of Aznalcollar (a.k.a. Los Frailes) (Alonso and Gens, 2006) or Cadia (Jefferies et al., 2019). Static liquefaction of tailings is possible if the tailings are deposited loose and remain saturated: these are frequently occurring features of the upstream construction method. Static liquefaction failure is a consequence of undrained strength brittleness (Bishop, 1973), a condition of some contractive materials in which undrained shearing goes through a peak before attaining critical state conditions at much lower stresses (Fig. 1). Such phenomenon results in fragile geotechnical structures, where failure can progress at a very fast pace—as illustrated by the Brumadinho case. Once liquefied, the material can flow long distances increasing the consequences of failure.

Classical stability analysis methods based on limit equilibrium are poorly adapted to incorporate brittle behaviour. Stress-deformation analyses have been systematically employed to analyse static liquefaction in recent large-scale failures (Morgenstern et al., 2015; Jefferies et al., 2019; Robertson et al., 2019) and are now quickly moving into industrial practice (Sottile et al., 2020; Valdivia et al., 2020; Boswell et al., 2020).

The constitutive model selected to represent tailing behaviour is a key element in this kind of analyses. Critical state soil mechanics offers a clear framework to understand static liquefaction (Jefferies and Been, 2016) and to formulate constitutive models that reproduce this behaviour. This approach was pioneered by the Nor-Sand model (Jefferies, 1993), which has been later updated and refined (Shuttle and Jefferies, 1998; Jefferies and Shuttle, 2011). Nor-Sand was, for instance, successfully employed to clarify the failure mechanism in the case of Fundão (Morgenstern et al., 2015). On the other hand, Robertson et al. (2019) had to abandon Nor-Sand numerical analyses of Brumadinho failure because of numerical instabilities.

In this work, we explore the use of a different constitutive model in the numerical analysis of tailings dam failure involving static liquefaction. The model formulation is briefly presented in the next section. A general procedure to facilitate calibration is then discussed. Finally, the approach presented is exemplified by performing a numerical analysis of the Merriespruit tailing dam failure. Fourie et al. (2001) identified tailings static liquefaction, triggered by overtopping induced erosion, as a major mechanism acting in the Merriespruit failure. To our knowledge, the work presented here is the first published stress-deformation analysis of that landmark case.

2 Constitutive description - CASM

A slightly modified version of the Clay And Sand constitutive Model (CASM) (Yu, 1998) is employed here to model the Merriespruit tailings. CASM was originally formulated as an

extension of classical critical state models such as the original (or modified) Cam Clay, explicitly incorporating the state parameter concept. By a suitable choice of parameters, CASM could represent both clays and sands (Yu, 1998); this makes it *a priori* a good candidate to model intermediate materials such as the silts and silty sands of which most tailings are made of. More important is perhaps the fact that CASM is capable of reproducing the undrained softening underlying the flow liquefaction phenomenon (Gens, 2019).

The state parameter ψ (Been and Jefferies, 1985) is defined as the difference between the current specific volume v and the specific volume on the critical state line (CSL) for the same effective mean stress p' (Fig. 2). The CSL in the compression plane $v - \ln p'$ is assumed linear, and has the following expression:

$$v = \Gamma - \lambda \ln p' \quad (1)$$

where Γ gives the specific volume on the CSL for $p' = 1$ kPa and λ is the slope of the CSL and reference consolidation lines in a $v - \ln p'$ plot (Fig. 2).

The state parameter provides information about the expected behaviour of the material under shearing. For instance, a positive value of ψ implies that before reaching the CSL, a volume contraction must take place under drained conditions, or, under undrained conditions, an increase of the pore-water pressure, i.e. a reduction of the mean effective stress.

In terms of ψ , the yield function of the CASM model is given by

$$f = \left(\frac{q}{p' M_\theta} \right)^n + \frac{\psi}{\psi_R} - 1 \quad (2)$$

where q is an invariant of the deviatoric stress tensor, M_θ is the slope of the CSL in the $q - p'$ space, n is a parameter that controls the shape of the yield function, and ψ_R is the reference state parameter defining the separation between the CSL and the reference consolidation line (Fig. 2). The yield function can also be expressed in terms of the isotropic yield stress p'_o and the spacing ratio r (see Fig. 2) as

$$f = \left(\frac{q}{p' M_\theta} \right)^n + \frac{1}{\ln r} \ln \frac{p'}{p'_o}. \quad (3)$$

Equation (3) is preferred here for the model implementation. The effect of n and r on the shape of the yield function is depicted in Fig. 3. Unlike the original or modified Cam Clay models, the critical state may not coincide with the highest point of the yield surface. This feature is, precisely, what allows the undrained softening behaviour previously mentioned.

Following Yu (2006), the shape of the yield function in the deviatoric plane is given by the following relation (Sheng et al., 2000):

$$M_\theta = M \left(\frac{2\alpha^4}{1 + \alpha^4 + \sin 3\theta - \alpha^4 \sin 3\theta} \right)^{1/4} \quad (4)$$

where M is the slope of the CSL under triaxial compression and α is a parameter controlling the difference of M_θ between triaxial compression and extension. To ease the determination

of parameters, α was selected to coincide with the Mohr-Coulomb envelope for those loading conditions, resulting in

$$\alpha = \frac{3}{3 + M}. \quad (5)$$

The adopted function in the deviatoric plane is depicted in Fig. 4 along with the Mohr-Coulomb envelope.

The CASM constitutive model uses the same strain hardening rule than the modified Cam Clay:

$$\frac{dp'_o}{d\epsilon_v^p} = \frac{p'_o v_{\text{ini}}}{\lambda - \kappa} \quad (6)$$

where ϵ_v^p is the volumetric plastic strain, v_{ini} is the initial specific volume, and κ is the unloading-reloading slope in a $v - \ln p'$ plot (see Fig. 2).

In the original CASM formulation, the plastic potential function was derived from the stress-dilatancy relationship of Rowe (1962). However, as pointed out by Yu (2006), Rowe's stress-dilatancy relation is not particularly realistic for stress paths with low stress ratios such as isotropic or one-dimensional consolidation. A new formulation for the plastic potential function was adopted here:

$$g = \left(\frac{q}{p' M_\theta} \right)^m + m - \frac{p'_c (m - 1)}{p'} - 1 \quad (7)$$

where m is a parameter controlling the shape of the function and p'_c must be solved for the current stress state.

Finally, the elastic behaviour is characterised by the typical Cam Clay non-linear elasticity, which results in a bulk modulus given by

$$K = \frac{p' v_{\text{ini}}}{\kappa}. \quad (8)$$

Then, the full elastic stiffness matrix is assembled by assuming a constant Poisson ratio ν .

The described version of the CASM constitutive model was implemented as a user-defined soil model in the finite element code Plaxis (Bentley Systems, 2020) which was used in the simulation of the case study described below.

3 CASM calibration for tailings

3.1 General approach

In the general case, eight parameters are employed (M , Γ , λ , κ , ν , n , r , and m) to describe a material in the implemented CASM. In addition, the material state needs initialisation, which, apart from the initial effective stress, would in principle require in CASM specifying the initial isotropic yield stress p'_o and the initial specific volume v_{ini} .

Of the required parameters, five (M , Γ , λ , κ , and ν) are relatively unproblematic, as they can be directly evaluated by well-established testing procedures—e.g. for CSL parameters M ,

Γ , and λ see Reid et al. (2020)—or, in some case, do not vary much and can reasonably be guessed (κ and ν). The difficulty lies in the other three parameters (n , r , and m), whose physical meaning appears not so clear *a priori*. It turns out, however, that they can be related to simple experimental measures.

Parameter m controls the plastic flow ratio and may be estimated from the coefficient of earth pressure at rest K_o . From the conditions imposed by an oedometer tests, a relationship can be established between m and K_o :

$$\frac{9(\lambda - \kappa)(2\nu - 1)}{2\kappa\eta_{K_o}(\nu + 1) + 6\lambda(2\nu - 1)} = \left(\frac{M}{m} - M\right) \frac{\eta_{K_o}}{M} + \left(M - \frac{M}{m}\right) \left(\frac{\eta_{K_o}}{M}\right)^{1-m} \quad (9)$$

where the stress obliquity ratio in one-dimensional consolidation η_{K_o} is given by

$$p'_{K_o} = \left(\frac{1 + 2K_o}{3}\right) \sigma'_v \quad q_{K_o} = (1 - K_o) \sigma'_v \quad \eta_{K_o} = \frac{3(1 - K_o)}{1 + 2K_o}. \quad (10)$$

where σ'_v is the effective vertical stress.

Tailings are frequently found in a normally consolidated state. That was the case, for instance, of the Merriespruit tailings (Wagener, 1997). For normally consolidated conditions CASM initialisation is greatly simplified, as the current stress lies on the yield surface and p'_o is fixed through Eq. (3) for any given set of parameters. Moreover, for normally consolidated materials, CASM formulation imposes that all constant η stress paths correspond to a unique state parameter value, given by

$$\psi = (\lambda - \kappa) \ln r \left[1 - \left(\frac{\eta}{M}\right)^n \right]. \quad (11)$$

If consolidation is isotropic, then $\psi = \psi_R$ (Fig. 2). For one-dimensional K_o consolidation, this expression will become:

$$\psi_{K_o} = (\lambda - \kappa) \ln r \left[1 - \left(\frac{\eta_{K_o}}{M}\right)^n \right]. \quad (12)$$

It is then preferred, if normally conditions are present, to initialise the material using the initial state parameter ψ_{ini} , instead of v_{ini} or e_{ini} , as those will generally vary with depth and also are very difficult to measure. Then, v_{ini} can be initialise in terms of ψ_{ini} as

$$v_{ini} = \psi_{ini} + \Gamma - \lambda \ln p'_{ini}. \quad (13)$$

Given a state parameter value, relation (11) establishes, for given values of M , λ , and κ , a link between parameters n and r . Another link is necessary and, as will be shown, it is readily available. However, it is first necessary to take a small detour.

3.2 Empirical description of peak undrained strength

As described by Gens (2019), while the final state after undrained softening is reasonably well established based on critical state considerations, there are less conceptual constraints

concerning the point of maximum undrained strength that signals the onset of instability. The correct characterisation of peak strength is of utmost importance in the context of stability computations, such as those addressed in this work. Perhaps the two most remarkable attempts for the rationalisation of the undrained peak strength, in materials exhibiting static (a.k.a. flow) liquefaction, are the concepts of the collapse line (Sladen et al., 1985; Ishihara, 1993) and the flow liquefaction line (Vaid and Chern, 1985; Lade, 1993). Both address the issue proposing an effective stress linear yield envelope to characterise peak conditions, but with the collapse line passing through the steady-state point (Fig. 5a) and the flow liquefaction line passing through the origin (Fig. 5b). The uniqueness of the lines in the stress space is assumed, although Yang (2002), considering the flow liquefaction line concept, argued that its slope depends on the state parameter.

Such linear criteria have proven useful for limit equilibrium calculations, but they are difficult to implement as calibration constraints in the context of numerical modelling since the resulting undrained peak strength will depend on the specific path by which the failure criterion is attained. A stronger calibration constraint, but at the same time quite straightforward from a practical perspective, is obtained if undrained peak conditions are characterised through a normalised undrained strength ratio.

For saturated clays, normalised undrained strength ratios are typically defined as

$$S = \frac{s_u}{\sigma'_{v\text{ini}}} \quad (14)$$

where s_u is the undrained strength and $\sigma'_{v\text{ini}}$ is the pre-shearing consolidation vertical effective stress. S has been used for a long time to characterise undrained strength in saturated clays (e.g. Henkel, 1960; Parry, 1960), and it is fairly well established that S is approximately a constant for a given clay and a given overconsolidation ratio (OCR) (Ladd, 1974).

Although S has not been generally associated with sands and non-plastic silts, it appears that it does also offer a good template description of undrained peak strength in materials exhibiting static liquefaction. From an implementation standpoint, the mean effective stress attained prior to shearing is preferred for normalisation and, therefore, the undrained strength ratio will be described by

$$S_p = \frac{s_{u\text{pk}}}{p'_{\text{ini}}} \quad (15)$$

where $s_{u\text{pk}}$ refers to the peak undrained strength.

Fig. 6a shows the relationship between the undrained peak strength and the consolidation mean effective stress p'_{ini} of undrained triaxial compression tests (isotropically and anisotropically consolidated) on several well-documented examples of sands, tailings, and silty gravels that showed flow liquefaction. It is evident that results can be approximated reasonably well by straight lines from the origin and, therefore, by S_p values.

One interesting aspect is that the value of S_p depends on the consolidation path. This was clearly demonstrated by Fourie and Tshabalala (2005) who tested different tailings retrieved from Merriespruit after either isotropic or anisotropic K_o consolidation. The results (e.g. Fig. 6b) show unequivocally that anisotropic consolidation results in larger S_p values than isotropic

consolidation. The likely reason for this difference (Fourie and Tshabalala, 2005; Nguyen et al., 2017) is the different fabrics that are created during the different consolidation paths. Therefore, S_p also provides an indirect way of accounting for fabric anisotropy, which is of particular interest for models, such as CASM, in which fabric does not feature explicitly.

3.3 Implementation into CASM

An undrained peak strength characterised in terms of S_p can be directly related to the parameters of the CASM constitutive model. To do so, we assume that the undrained peak strength is reached when the stress state is at the highest point of the yield surface. It can be shown that the stress ratio at this point is given by

$$\eta_{\text{pk}} = \frac{q_{\text{pk}}}{p'_{\text{pk}}} = \frac{M_{\theta}}{\sqrt[n]{n \ln r}} \quad (16)$$

where q_{pk} is defined in terms of the undrained strength ratio:

$$q_{\text{pk}} = 2S_p p'_{\text{ini}} . \quad (17)$$

Note, however, that the position of the yield surface when the stress state reaches the highest point is not the same as the initial position after consolidation (see Fig. 7). During undrained loading, the total volume remains constant. The reduction of the effective mean stress, observed in loose materials, is accompanied by an elastic volume expansion, which is compensated by a plastic compression and some hardening.

It is assumed here that the material is normally consolidated and, therefore, the initial stress state lies on the yield surface. Thus, the initial value of p'_o can be derived from the yield criterion (Eq. 3) as follow:

$$p'_{o \text{ ini}} = p'_{\text{ini}} \exp \left[\left(\frac{\eta_{\text{ini}}}{M_{\theta}} \right)^n \ln r \right] . \quad (18)$$

At peak, the stress state remains on the yield surface and, therefore, a similar relation holds:

$$p'_{o \text{ pk}} = p'_{\text{pk}} \exp \left[\left(\frac{\eta_{\text{pk}}}{M_{\theta}} \right)^n \ln r \right] . \quad (19)$$

Furthermore, since the total volume remains constant during undrained loading, elastic and plastic volumetric deformations must have the same magnitude but opposite signs:

$$(\lambda - \kappa) \ln \left(\frac{p'_{o \text{ pk}}}{p'_{o \text{ ini}}} \right) = -\kappa \ln \left(\frac{p'_{\text{pk}}}{p'_{\text{ini}}} \right) . \quad (20)$$

By substituting Eq. (16) to (19) into (20) the following expression may be derived:

$$\exp \left[\left(\frac{1}{\sqrt[n]{n \ln r}} \right)^n \ln r \right] = \frac{M}{2S \sqrt[n]{n \ln r}} \exp \left[\left(\frac{\eta_{\text{ini}}}{M} \right)^n \ln r \right] \exp \left[\frac{\kappa}{\lambda - \kappa} \ln \left(\frac{M}{2S \sqrt[n]{n \ln r}} \right) \right] . \quad (21)$$

This offers a complementary relation between unknown parameters r and n to that described by Eq. (11). An iteration procedure is necessary to determine the two parameters. A first

estimate for the value of r can thus be obtained neglecting the terms in brackets in Eq. (11), then obtaining an n value with (21) and iterating the procedure until convergence. It will be noted that this procedure makes some model parameters (n and r) dependent on the initial state of the material (ψ_{ini}). This reflects an intrinsic limitation of the model—namely that anisotropy is not directly represented—and is also a feature of other isotropic models like Nor-Sand (Shuttle and Jefferies, 1998). This limitation does not represent a serious hindrance for application, as demonstrated in the following section.

4 Case study - Merriespruit tailings dam failure

4.1 Overview of the case

On 22 February 1994, a portion of the northern wall of compartment 4A in the Merriespruit dam failed, resulting in some 600,000 m³ of liquid slime rushing through the town causing the death of 17 people and a major environmental disaster. A detailed account of the Merriespruit tailing dam construction, operation, and failure can be found in Wagener (1997), Wagener et al. (1998), Strydom and Williams (1999), and Fourie et al. (2001). Only a brief extract of that account is given here, with help from a cross-section through the northern wall of the dam that illustrates the sequence leading to dam failure (Fig. 8).

The dam, started in 1978, was built using the *upstream semi-dry paddock* method, a common technique for gold tailings in South Africa. In this technique, a starter dam and blanket drains are initially constructed. The dam is then raised by constructing the so-called *daywall* using a perimeter paddock. This is 10 to 50 m wide and is filled by sections during daily operation in 15 to 20 cm lifts which are then left to dry for 10 to 14 days. The paddock walls are then raised using the dried tailings. In the main body of the dam, surrounded by the paddock, tailing deposition takes place during the night, creating a beach and a pool from which excess water is decanted outside the dam through a penstock. Within this concept, stability of the dam relies on the presence of the dry material in the paddock, on effective underdrainage, and on an adequate distance of the inner decanting pool to the daywall. All of these features were found at fault in Merriespruit (Wagener, 1997; Fourie et al., 2001). The underdrain was not performing well, the daywall was constructed with tailings that were too wet, and the tailing deposition arrangements resulted in a pool that was too close to the paddock. These construction malfunctions were particularly intense near the section that was to fail (2 and 4 in Fig. 8a). Seepage and sloughing in the outer wall were common in that section, so much so that a slime buttress (5 in Fig. 8a) was constructed aiming to stabilise the lower slope. Eventually, a decision was made to stop deposition at compartment 4A.

The stoppage decision was, however, not effectively enforced. Excess water from the plant was still being delivered to compartment 4A. This water pushed against the pool close to the northern wall and reduce the outer wall freeboard to unacceptable levels (2 in Fig. 8a). Sloughing continued at the lower slope and local slips occurred immediately above the buttress shortly before the disaster. They were repaired by dozing in dry slime from the lower berm (6, 7, and 8 in Fig. 8a).

A few hours before the failure, a thunderstorm took place. Due to insufficient freeboard, rainfall caused overtopping on the northern wall. The spilling water eroded loose slimes placed, due to earlier slips, on the lower slope in turn causing more small slip failures (Fig. 8b). This led to a series of progressive failures moving up the slope and resulting in the massive overall slope failure (Fig. 8c).

The failure was surprising because previous overtopping incidents in similar dams had resulted in erosion gullies, but not in mass failure. The large flowslide was also surprising as it evidenced liquefied behaviour: based on generally observed dilatant behaviour in the lab, it was thought that gold tailings were not liquefiable.

Fourie et al. (2001) convincingly demonstrated that the Merriespruit tailings were indeed liquefiable. They noted that 30% of tailing samples had resulted in void ratios above 1.2. They used CSL established by Fourie and Papageorgiou (2001) on reconstituted moist tamped specimens to estimate state parameter values. They concluded that the finer fraction of tailings (those with at least 60% fines) was dominated by positive values of ψ_{ini} and was therefore contractive and liquefiable. Finer tailings were likely to be present in the breach zone because of the pool management problems noted above.

Fourie et al. (2001) endorsed the failure sequence presented by Wagener (1997). Overtopping occurred first, producing slope erosion and localised failures that increased in size. The detail of that sequence is, however, not fully clear. For instance: how much erosion was necessary to initiate liquefaction in the tailings? Fourie et al. (2001) noted that loud bangs were heard just before the mudflow overcome the village, suggesting the sudden collapse of a large tailing volume. How large was that volume? A stress-deformation analysis is useful to answer that kind of questions as exemplified in the following sections.

4.2 Relevant laboratory tests

Fourie and Tshabalala (2005) report an experimental campaign comprising a number of isotropically and anisotropically (K_o) consolidated triaxial compression tests on reconstituted specimens from material retrieved from the Merriespruit dam. Samples were prepared with fine contents (FC) of 0, 20, 30, and 60% resulting in somewhat different critical state lines.

As reported by Fourie et al. (2001), most of the samples recovered from locations close to the failure scarp had fines contents larger than 50% and, therefore, the test series with 60% of fines were adopted here. In addition, only the K_o consolidated tests are considered here, as they are believed to represent better in situ conditions than isotropic tests (Fourie and Tshabalala, 2005). The stress paths and state diagram resulting from this test series are shown in Fig. 9a and Fig. 10a respectively. The test results demonstrate the potential for static liquefaction of this material. Although a couple of samples showed partial liquefaction and phase transformation, the increase of deviatoric stress was quite limited and subsequent to major strength loss.

Parameters Γ , λ , M , S_p , and K_o (Table 1) were directly determined from these laboratory data. No information was available for κ and ν and, therefore, they were assumed equal to 0.01 and 0.3 respectively. A value of m was then derived using Eq. (9) (Table 1).

For validation, the selected triaxial tests results were simulated with CASM. For these purpose, the initial state parameter ψ_{ini} was derived from the adjusted critical state line and the initial void ratio of each specimen (shown in Fig. 9a). Values of n and r were derived as described in Section 3. Since ψ_{ini} values differ somewhat between samples, different r and n were computed for each of them. Table 2 summarises the values of ψ_{ini} , n and r for each specimen.

Simulation results are compared with laboratory data in terms of the stress paths, state diagrams, and undrained peak strengths in Fig. 9, 10, and 11 respectively. The results show that CASM is able to capture the observed laboratory behaviour, including the undrained peak strength and the critical states in the $q - p'$ and $v - \ln p'$ planes.

4.3 Numerical model of the dam

A section of the Merriespruit tailing dam was simulated through a two-dimensional plane strain finite element analysis with Plaxis (Bentley Systems, 2020). Geometry was derived from the critical section sketched in Wagener (1997) (Fig. 8), which was part of the northern wall where failure took place. The geometry, boundary conditions, and finite element mesh employed are shown in Fig. 12. The mesh comprises 1190 triangular finite elements with fourth-order interpolation and 12 integration points.

The geometry incorporates a portion of the lower slope that is later removed in order to simulate the erosion caused by overtopping. The assumed position of the phreatic surface corresponds to that sketched by Wagener (1997) (Fig. 8). Nevertheless, even above the phreatic surface, tailings are assumed saturated. This is thought reasonable as the presence of pool water close to the inner paddock wall (Fig. 8a) in the days preceding the failure is well-documented (Strydom and Williams, 1999).

The model only includes two materials: the gold tailings and the starter dam. Properties of the starter dam material are not reported in the available descriptions. It is assumed here to be formed with a competent, not liquefiable granular material. This is characterised using an elastic perfectly plastic Mohr-Coulomb model, with the parameters shown in Table 3.

The gold tailings were modelled with CASM, using the same parameters as those derived for the simulation of the triaxial tests (Table 1). The exception was the initial state parameter and those parameter values (n and r) that derive from it. Much larger values of ψ_{ini} than those resulting from the reconstitution of specimens in Fourie and Tshabalala (2005) were reported by Fourie et al. (2001) from nominally undisturbed samples obtained during post-failure investigations. More than 85% of the samples with more than 60% fines were assigned ψ_{ini} values of 0.1 or greater, up to values of 0.8. These values were estimated by Fourie et al. (2001) under the assumption that the CSL position obtained for 60% FC tailings would also apply at higher FC. It is now known that this is not always the case and, for instance, Smith et al. (2019) present evidence indicating that 60% FC might actually correspond to the lowermost position of the CSL. Considering all this, a ψ_{ini} value of 0.1 was adopted in the simulation as a reasonably conservative choice for the tailings in the Dam. The values of n and r corresponding

to the assumed ψ_{ini} are 5.16 and 151.5 respectively.

A detailed timeline of the dam elevation—including, for instance, a historical record pond extents—was not available and, therefore, a realistic simulation of dam construction was not feasible. Initial static equilibrium was thus established directly on the pre-failure geometry using a Mohr-Columb material for tailings. This material had null cohesion and a friction angle value chosen so that the initial stress state at any point lied below the effective stress instability line ($\phi = 26.2$) (Fourie and Tshabalala, 2005) as well as a Poisson ratio corresponding to the assumed coefficient of earth pressure at rest: $\nu = K_o/(1 + K_o)$. In a second stage, the tailing material was substituted by CASM assuming drained conditions. As expected, the material change resulted in a stable condition in the simulation.

Finally, dam erosion due to overtopping was simulated by removing the portion of the geometry indicated in Fig. 12. As in many finite element codes that can address non-linear behaviour, this removal is done by substituting the material for the corresponding equilibrium nodal forces at the new boundary and then progressively reducing those forces until failure occurs which is indicated by an inability of the solution to achieve convergence. This progressive reduction is indicated through the force reduction factor (FRF), defined as one minus the ratio between the current and initial value of those forces. The removal of the eroded material was performed assuming undrained conditions since failure occurred in a matter of a few hours after overtopping initiated and the tailings permeability was low.

4.4 Results of the analysis

The analysis phase corresponding to the removal of the eroded material was not completed as a condition of general failure—i.e. a state of equilibrium could not be achieved—was attained in the simulation with just a $\text{FRF}=0.15504$. This result indicates that the removal of a smaller portion of tailings would have already failed the slope. This is in line with the perception expressed by Fourie et al. (2002), that only a very small trigger would have been necessary to unleash failure. The failure mechanism can be clearly identified in Fig. 13 in terms of the deformed mesh and contours of incremental displacements (norm) at failure. An approximately circular failure surface was obtained, passing above the starter dam.

Fig. 14 shows contours of the incremental deviatoric strain invariant ϵ_q at different steps during the removal of the eroded material. In the beginning, deviatoric deformations are small and widely spread around the eroded area. However, as seen in Fig. 9, only a moderate increase in deviatoric stresses is required to push the liquefiable tailings into an unstable condition. Such instability did not occur simultaneously in a large portion of the domain, but it initiated in a small area below the eroded zone, close to the foundation, where ϵ_q starts to accumulate significantly in the form of a shear band. As liquefaction starts and undrained softening takes place, this inevitably leads to a progressive failure condition where the occurrence of liquefaction at a given Gauss point induces liquefaction at neighbouring points. This results in the propagation of liquefaction and the progressive evolution of the shear band upward until it finds an exit point and forms a kinematically admissible failure surface. It is worth noting that the shear band propagates progressively with the increase of the FRF. However, when reaching $\text{FRF} =$

0.155, a global instability takes place and the shear band propagates rapidly with a minimal increase in the load advancement procedure.

The failed block defined by the analyses has a surface of about 950 m². Considering that the breach observed post-failure was about 80 m wide at the wall, the analysis indicates that the first large failure may have already involved a significant fraction of the total failed volume. Failure of the block will reduce the confinement in the tailings left behind and most likely result in the formation of a new failure surface, repeating the process shown in Fig. 14, and resulting in the domino effect sketched by Wagener (1997) in Fig. 8c. However, representing the large displacements and deformations involved in that sequence of failures is something beyond the capabilities of the standard finite element formulation employed here, requiring instead tools such as the particle finite element method (e.g. Zhang et al., 2018; Monforte et al., 2019) or the material point method (e.g. Soga et al., 2016; Yerro et al., 2019).

The liquefied condition along the failure surface can be clearly identified in the contour plots shown in Fig. 15, corresponding to a FRF of 0.15504. Pore-water pressure increases occur within the shear band as the material moves towards critical state conditions (Fig. 15a). In fact, critical state (i.e. a near-zero ψ value) was very closely attained along the entire failure surface, as demonstrated in Fig. 15b. Although the critical state friction angle is rather large ($\phi_{sc} = 38.2^\circ$), the pore-water pressure increases result in p' values within the shear band nearly equal to zero (Fig. 15c). The soil in the shear band has lost the capacity to sustain any shear stress (Fig. 15d). Although a runout analysis (McDougall, 2017) is beyond the scope of this work, it is worth noting that the low post-liquefied strength and the relatively large height of the failed block are features that will be conducive to large runouts, as they were indeed observed in this case.

The liquefied condition along the failure surface can also be observed in Fig. 16, showing the stress paths at the Gauss points whose position is indicated in Fig. 15c, i.e. along the shear band. The figure also shows the evolution of the FRF for the corresponding points in the stress paths (Fig. 16b). Since both horizontal axes of Fig. 16 are the same, it is easy to identify the corresponding FRF for each data point in the stress paths. Points c and d, which are closer to the zone where liquefaction starts, showed softening behaviour since the beginning of the phase while points a and b, further away from that zone, showed an increase of deviatoric stresses before encountering flow liquefaction. The initial softening behaviour of points c and d occurred in a somewhat controlled manner. This is due to the fact that instability of a number of Gauss points does not necessarily imply a global instability, and the remaining points, still not in a softening regime, contribute to the global stability of the boundary value problem (Mánica et al., 2018). However, once this global instability takes place, softening accelerates remarkably, propagating the shear band to points a and b and driving all points to critical state conditions with a minimal increase in the FRF.

5 Discussion

A single value of ψ_{ini} for all tailing materials might seem a gross simplification, since ψ_{ini} is expected to show spatial variability due to the construction method, varying conditions of

the slimes in time, and segregation induced during discharge. Besides, as already noted, the estimates of field ψ_{ini} available for the Merriespruit tailings carry significant uncertainty. The analysis of the dam was thus repeated using a value of $\psi_{\text{ini}} = 0.046$ (and corresponding values of $n = 3.6$ and $r = 10.6$), corresponding to the larger value of the reconstituted experiments (Table 2), but still at the lower limit of the field estimates provided by Fourie et al. (2001). The dam failed in exactly the same manner as before, although now the reduction in weight of the eroded zone at failure was slightly higher, with a FRF of 0.22.

Geotechnical modelling is always beset by the conflict between simplicity and oversimplification (Wood, 1991). The CASM variant that is used here has a number of important limitations: it cannot handle phase transformation, it does not represent bonding, it does not represent anisotropy (fabric dependent or not), and it is not adequate for cyclic loading. Some of these limitations are overcome by already available alternative CASM formulations: for instance, Yu et al. (2005) proposed a CASM variant to address phase transformation, González et al. (2009) a variant to address bonding (C-CASM), etc. Clearly, such model extensions always come with the price of more parameters, but simple calibration might still be feasible (e.g. for C-CASM see Arroyo et al., 2012).

Incorporation of anisotropy will require a more elaborate revamping of CASM, which—to our knowledge—is not yet available. The conceptual basis for such generalisations are well established (Gajo and Wood, 1999; Dafalias and Manzari, 2004; Karstunen and Koskinen, 2008, e.g.). It is also clear that calibration and initialisation problems are significantly increased for this kind of model, although efforts to address this problem are ongoing (Amorosi et al., 2021). Until such developments take place, the pragmatic alternative is to be aware of this limitation and incorporate indirectly the effect of consolidation derived anisotropy. This was done here by choosing S_p on K_o consolidated specimens and by allowing parameters n and r to be dependent on initial state.

Bearing in mind those limitations, as well as the assumption of a normally consolidated state, the practical appeal of the calibration procedure presented is evident. Thanks to the efforts of Jefferies, Been, and co-workers, critical state parameters and the state parameter itself are nowadays familiar to most tailing engineers. Apart from that, calibration of the CASM variant presented here only requires parameters that are either familiar, such as K_o , or have a very direct interpretation, such as S_p .

For the application case at Merriespruit, an outstanding laboratory campaign was available, whereas the in situ test results available (Wagener, 1997) were of more limited quality—CPTu lacking side friction data. In most cases today the situation will be likely different, with in situ tests dominating. The calibration procedure proposed can easily obtain key inputs from in situ tests. There are well-known empirical relations to derive stress normalised undrained peak strength ratios from CPTu (e.g. Olson and Stark, 2003). Similarly, Marchetti DMT results can be employed to evaluate K_o (e.g. Arroyo et al., 2015). As for the state parameter, a variety of approaches based on CPTu are already available, either empirical (e.g. Plewes et al., 1992) or based on cavity expansion methods (Shuttle and Jefferies, 2016). State and parameter identification may be also facilitated by realistic simulation of CPTu penetration with CASM, something now possible with advanced numerical technology (e.g. Monforte et al., 2021).

Finally, it is worth noting that, since static liquefaction involves strain softening and progressive failure, mesh dependence issues may prove important in the numerical simulation of this phenomenon. While not addressed in this work, this is currently a topic of active research (Mánica et al., 2018; Monforte et al., 2019).

6 Summary and conclusion

This paper presents the application of CASM, a critical state constitutive model, in a stress-deformation analysis of the Merriespruit tailings dam failure. The model naturally incorporates the undrained softening behaviour underlying the static liquefaction phenomenon observed in saturated loose tailings. A novel approach for the selection of parameters is presented using the normalised undrained peak strength ratio. This concept, well-known from applications in clay, appears useful also for loose tailings and other materials exhibiting static liquefaction. Through the described approach, characterisation of the material is done in terms of familiar inputs that can be determined from conventional laboratory or field procedures.

The analysis of Merriespruit confirms that, as previously speculated, a large slide could be triggered in the liquefiable tailings by the erosion, due to overtopping, of a relatively small portion of the impoundment wall. Static liquefaction only occurs under undrained or partially undrained conditions (both in CASM and in reality). Although in the Merriespruit case the simulations assumed undrained conditions due to the rapid erosion that took place, the approach presented is more general. CASM is an effective stress model which can be used, in fully-coupled hydro-mechanical analyses, to explore if and when undrained conditions may arise in tailings dams due to factors such as construction/intervention times, transient hydraulic conditions, or atmospheric interactions. It is hoped that the generalisation of that kind of analysis in the future will contribute to reduce the rate of failure of those important and necessary structures.

Notation

e_{ini}	Initial void ratio
K	Bulk modulus
FRF	Force reduction factor
K_o	Coefficient of earth pressure at rest
M	Slope of the CSL in the $q - p'$ space for triaxial compression
M_θ	Slope of the CSL in the $q - p'$ space that depends on Lode angle
m	Parameter in the plastic potential function
n	Parameter in the yield function
p'	Effective mean stress
p'_{K_o}	Effective mean stress for one-dimensional consolidation
p'_c	Constant in the plastic potential function
p'_o	Isotropic yield stress

q	Invariant of the deviatoric stress tensor
q_{K_o}	Invariant of the deviatoric stress tensor for one-dimensional consolidation
r	Spacing ratio
S	Undrained strength ratio
S_p	Undrained strength ratio for peak conditions and normalised with p'_{ini}
s_u	Undrained shear strength
$s_{u\text{pk}}$	Undrained peak shear strength
v	Specific volume
v_{ini}	Initial specific volume
α	Parameter controlling the shape of the yield function in the deviatoric plane
Γ	Specific volume on the CSL for $p' = 1$ kPa
ϵ_q	Deviatoric strain invariant
ϵ_v^p	Volumetric plastic strain
η	Stress obliquity ratio
η_{K_o}	Stress obliquity ratio for one-dimensional consolidation
θ	Lode angle
κ	Unloading-reloading slope in a $v - \ln p'$ plot
λ	Slope of the CSL in a $v - \ln p'$ plot
ν	Poisson ratio
σ'_v	Effective vertical stress
$\sigma'_{v\text{ini}}$	Pre-shearing consolidation vertical effective stress
ϕ	Friction angle
ϕ_{sc}	Critical state friction angle
ψ	State parameter
ψ_{K_o}	State parameter for one-dimensional consolidation
ψ_R	Reference state parameter

References

- Alonso, E. E. and Gens, A. (2006). Aznalcóllar dam failure. Part 3: Dynamics of the motion. *Géotechnique*, 56(3):203–210.
- Amorosi, A., Rollo, F., and Dafalias, Y. F. (2021). Evolving elastic and plastic fabric anisotropy in granular materials: theoretical and applied implications. In *International Conference of the International Association for Computer Methods and Advances in Geomechanics*, pages 691–698. Springer.
- Arroyo, M., Amoroso, S., Devincenzi, M., and Pérez, N. (2015). In-situ testing of a cement-stabilized metallurgical residue. In *3rd International Conference on the Flat Dilatometer*, Rome, Italy.

- Arroyo, M., Ciantia, M. O., Castellanza, R., Gens, A., and Nova, R. (2012). Simulation of cement-improved clay structures with a bonded elasto-plastic model: A practical approach. *Computers and Geotechnics*, 45:140–150.
- Been, K. (2016). Characterizing mine tailings for geotechnical design. *Australian Geomechanics Journal*, 51(4):59–78.
- Been, K. and Jefferies, M. G. (1985). A state parameter for sands. *Géotechnique*, 35(2):99–112.
- Bentley Systems (2020). PLAXIS CONNECT Edition 20.04.
- Bishop, A. W. (1973). The stability of tips and spoil heaps. *Quarterly Journal of Engineering Geology and Hydrogeology*, 6:335–376.
- Boswell, J., Sobkowicz, J., Gidley, I., Rentz, A., and Schmidt, C. (2020). Responsible design and other defences against static liquefaction of tailings structures. In *Proceedings of Tailings and Mine Waste 2019*, pages 45–60, Vancouver. University of British Columbia.
- Dafalias, Y. F. and Manzari, M. T. (2004). Simple plasticity sand model accounting for fabric change effects. *Journal of Engineering mechanics*, 130(6):622–634.
- Davies, M., Martin, D., and P, L. (2001). Tailings dam stability - essential ingredients for success. In Hustrulid, W. A., McCarter, M. K., and Van Zyl, D. J. A., editors, *Slope stability in surface mining*, chapter 40, pages 365–378. Society for Mining, Metallurgy, and Exploration, Inc.
- Davies, M. P. (2002). Tailings impoundment failures: are geotechnical engineers listening? *Geotechnical News*, (September).
- Fourie, A. B., Blight, G. E., and Papageorgiou, G. (2001). Static liquefaction as a possible explanation for the Merriespruit tailings dam failure. *Canadian Geotechnical Journal*, 38(4):707–719.
- Fourie, A. B., Blight, G. E., and Papageorgiou, G. (2002). Static liquefaction as a possible explanation for the Merriespruit tailings dam failure: Reply. *Canadian Geotechnical Journal*, 39(6):1441–1442.
- Fourie, A. B. and Papageorgiou, G. (2001). Defining an appropriate steady state line for Merriespruit gold tailings. *Canadian Geotechnical Journal*, 38(4):695–706.
- Fourie, A. B. and Tshabalala, L. (2005). Initiation of static liquefaction and the role of Ko consolidation. *Canadian Geotechnical Journal*, 42(3):892–906.
- Franks, D. M., Stringer, M., Baker, E., Valenta, R., Torres-Cruz, L. A., Thygesen, K., Matthews, A., Howchin, J., and Barrie, S. (2020). Lessons from tailings facility data disclosures. In Oberle, B., Brereton, D., and Mihaylova, A., editors, *Towards Zero Harm: A Compendium of Papers Prepared for the Global Tailings Review*, pages 84–108. Global Tailings Review, London.

- Gajo, A. and Wood, M. (1999). Severn–Trent sand: a kinematic-hardening constitutive model: the q–p formulation. *Géotechnique*, 49(5):595–614.
- Gens, A. (2019). Hydraulic fills with special focus on liquefaction. In Sigursteinsson, H., Erlingsson, S., and Bessason, B., editors, *Proc. XVII European conference on soil mechanics and geotechnical engineering*, pages 1–31, Reykjavik. The Icelandic Geotechnical Society.
- Giurco, D., Dominish, E., Florin, N., Watari, T., and McLellan, B. (2019). Requirements for minerals and metals for 100% renewable scenarios. In Teske, S., editor, *Achieving the paris climate agreement goals*, chapter 11, pages 437–457. Springer International Publishing, Cham.
- González, N. A., Arroyo, M., and Gens, A. (2009). Identification of bonded clay parameters in SBPM tests: a numerical study. *Soils and Foundations*, 49(3):329–340.draw
- Henkel, D. J. (1960). The shear strength of saturated remolded clays. In *Proc. ASCE specialty conference on shear strength of cohesive soils*, pages 533–554, Boulder, Colorado. University of Colorado.
- International Council on Mining & Metals (ICMM), Principles for Responsible Investment (PRI), and United Nations Environment Programme (UNEP) (2020). Global industry standard on tailings management. Technical report.
- Ishihara, K. (1993). Liquefaction and flow failure during earthquakes. *Géotechnique*, 43(3):351–451.
- Jefferies, M. and Been, K. (2016). *Soil liquefaction: A critical state approach*. CRC Press, Taylor & Francis, Boca Raton, FL, USA, 2nd edition.
- Jefferies, M., Morgenstern, N. R., Van Zyl, D. V., and Wates, J. (2019). Report on NTSF Embankment Failure. Technical report, Valley Operations for Ashurst Operations., South Orange, NSW, Australia.
- Jefferies, M. and Shuttle, D. (2011). On the operating critical friction ratio in general stress states. *Géotechnique*, 61(8):709–713.
- Jefferies, M. G. (1993). Nor-Sand: a simple critical state model for sand. *Géotechnique*, 43(1):91–103.
- Karstunen, M. and Koskinen, M. (2008). Plastic anisotropy of soft reconstituted clays. *Canadian Geotechnical Journal*, 45(3):314–328.
- Ladd, C. C. (1974). New design procedure for stability of soft clays. *Journal of the Geotechnical Engineering Division*, 100(GT7):763–786.
- Lade, P. V. (1993). Initiation of static instability in the submarine Nerlerk Berm. *Canadian Geotechnical Journal*, 30(6):895–904.
- Mánica, M. A., Gens, A., Vaunat, J., and Ruiz, D. F. (2018). Nonlocal plasticity modelling of strain localisation in stiff clays. *Computers and Geotechnics*, 103:138–150.

- McDougall, S. (2017). 2014 Canadian Geotechnical Colloquium: Landslide runout analysis — current practice and challenges. *Canadian Geotechnical Journal*, 54(5):605–620.
- Monforte, L., Ciantia, M. O., Carbonell, J. M., Arroyo, M., and Gens, A. (2019). A stable mesh-independent approach for numerical modelling of structured soils at large strains. *Computers and Geotechnics*, 116.
- Monforte, L., Gens, A., Arroyo, M., Mánica, M., and Carbonell, J. M. (2021). Analysis of cone penetration in brittle liquefiable soils. *Computers and Geotechnics*, (under review).
- Morgenstern, N. R. (2018). Geotechnical risk, regulation, and public policy. *Soils and Rocks*, 41(2):107–129.
- Morgenstern, N. R., Vick, S. G., Viotti, C. B., and Watts, B. D. (2015). Fundão Tailings Dam Review Panel: Report on the immediate causes of the failure of Fundao dam. Published online at <http://fundaoinvestigation.com/>.
- Nguyen, H. B. K., Rahman, M. M., and Fourie, A. B. (2017). Undrained behaviour of granular material and the role of fabric in isotropic and Ko consolidations: DEM approach. *Géotechnique*, 67(2):153–167.
- Olson, S. M. and Stark, T. D. (2003). Yield strength ratio and liquefaction analysis of slopes and embankments. *Journal of Geotechnical and Geoenvironmental Engineering*, 129(8):727–737.
- Parry, R. H. G. (1960). Triaxial compression and extension tests on remolded saturated clay. *Géotechnique*, 10(4):166–180.
- Plewes, H. D., Davies, M. P., and Jefferies, M. G. (1992). CPT based screening procedure for evaluating liquefaction susceptibility. In *Proceedings of the 45th Canadian Geotechnical Conference*, pages 1–9, Toronto. Canadian Geotechnical society.
- Reid, D., Fourie, A., Ayala, J. L., Dickinson, S., Ochoa-Cornejo, F., Fanni, R., Garfias, J., Da Fonseca, A. V., Ghafghazi, M., Ovalle, C., Riemer, M., Rismanchian, A., Olivera, R., and Suazo, G. (2020). Results of a critical state line testing round robin programme. *Géotechnique*, (in press).
- Robertson, P., de Melo, L., Williams, D. J., and Wilson, G. W. (2019). Report of the expert panel on the technical causes for the failure of Feijão Dam. Published online at <http://www.bltechnicalinvestigation.com/>.
- Rowe, P. W. (1962). The stress-dilatancy relation for static equilibrium of an assembly of particles in contact. *Proceedings of the Royal Society of London A*, 269(1339):500–527.
- Sheng, D., Sloan, S. W., and Yu, H. S. (2000). Aspects of finite element implementation of critical state models. *Computational Mechanics*, 26(2):185–196.
- Shuttle, D. and Jefferies, M. (1998). Dimensionless and unbiased CPT interpretation in sand. *International Journal for Numerical and Analytical Methods in Geomechanics*, 22(5):351–391.

- Shuttle, D. and Jefferies, M. (2016). Determining silt state from CPTu. *Geotechnical Research*, 3(3):90–118.
- Sladen, J. A., D'Hollander, R. D., and Krahn, J. (1985). The liquefaction of sands, a collapse surface approach. *Canadian Geotechnical Journal*, 22(4):564–578.
- Smith, K., Fanni, R., Chapman, P., and Reid, D. (2019). Critical state testing of tailings: comparison between various tailings and implications for design. In *Proceedings of Tailings and Mine Waste 2019*, pages 1183–1195, Vancouver. University of British Columbia.
- Soga, K., Alonso, E., Yerro, A., Kumar, K., and Bandara, S. (2016). Trends in large-deformation analysis of landslide mass movements with particular emphasis on the material point method. *Geotechnique*, 66(3):248–273.
- Sottile, M. G., Cueto, I. A., and Sfriso, A. O. (2020). A simplified procedure to numerically evaluate triggering of static liquefaction in upstream-raised tailings storage facilities. arXiv:2010.11705[physics.geo-ph].
- Strydom, J. H. and Williams, A. A. B. (1999). A review of important and interesting technical findings regarding the tailings dam failure at Merriespruit. *Journal of the South African Institution of Civil Engineering*, 41(4):1–9.
- Vaid, Y. P. and Chern, J. C. (1985). Cyclic and monotonic undrained response of saturated sands. In Khosla, V., editor, *Advances in the art of testing soils under cyclic conditions*, pages 120–147, Detroit. American Society of Civil Engineers.
- Valdivia, M., Quispe, R., Negrón, J., Ayala, R., and Parra, D. (2020). Numerical modelling of a mine waste dump-heap leach pad with different constitutive models. In *Proceedings Tailings and Mine Waste 2020*, pages 91–102.
- Wagener, F. (1997). The Merriespruit slimes dam failure: overview and lessons learned. *Journal of the South African Institution of Civil Engineering*, 39(3):11–15.
- Wagener, F., Craig, H. J., Blight, G. E., McPhail, G., Williams, A. A. B., and Strydom, J. H. (1998). The Merriespruit tailings dam failure - A review. In *Proceedings of the Conference on Tailings drawand Mine Waste '98*, pages 925–952, Fort Collins. Colorado State University.
- Wood, D. M. (1991). *Soil Behaviour and Critical State Soil Mechanics*. Cambridge University Press.
- Yang, J. (2002). Non-uniqueness of flow liquefaction line for loose sand. *Geotechnique*, 52(10):757–760.
- Yerro, A., Soga, K., and Bray, J. (2019). Runout evaluation of Oso landslide with the material point method. *Canadian Geotechnical Journal*, 56(9):1304–1317.
- Yu, H. S. (1998). CASM: a unified state parameter model for clay and sand. *International Journal for Numerical and Analytical Methods in Geomechanics*, 22(8):621–653.

- Yu, H. S., Khong, C. D., Wang, J., and Zhang, G. (2005). Experimental evaluation and extension of a simple critical state model for sand. *Granular Matter*, 7(4):213–225.
- Yu, H.-S. H.-S. (2006). *Plasticity and geotechnics*. Springer US, New York.
- Zhang, X., Sloan, S. W., and Oñate, E. (2018). Dynamic modelling of retrogressive landslides with emphasis on the role of clay sensitivity. *International Journal for Numerical and Analytical Methods in Geomechanics*, 42(15):1806–1822.

Figures

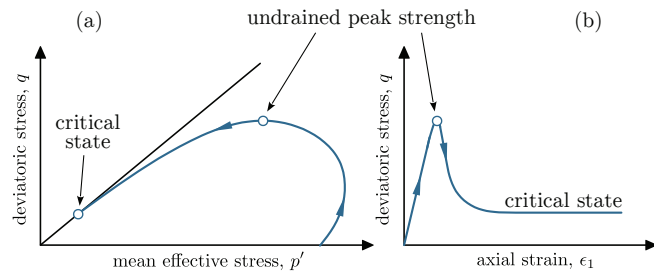


Figure 1: Undrained softening: (a) effective stress path and (b) stress-strain curve.

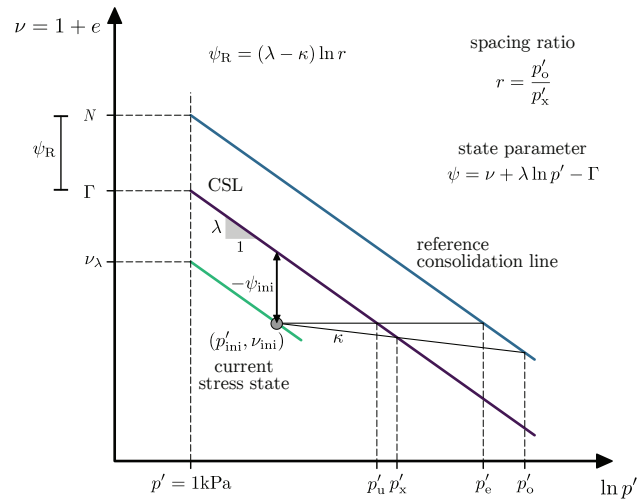


Figure 2: Definitions of CASM (modified from Yu, 1998)

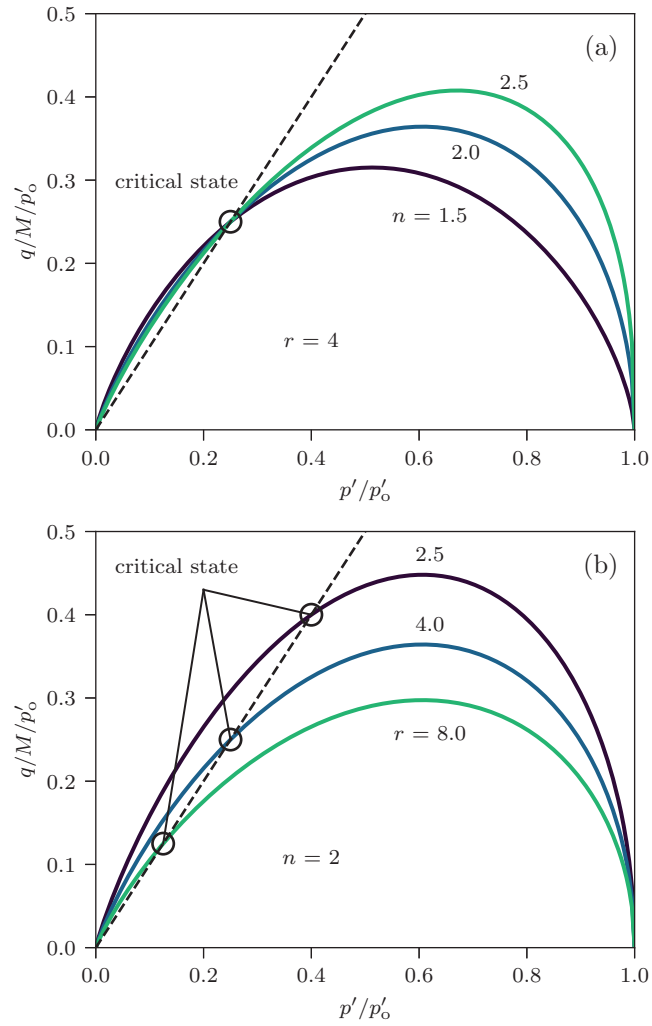


Figure 3: Normalised yield surfaces from CASM for different values of (a) n and (b) r (modified from Yu, 1998)

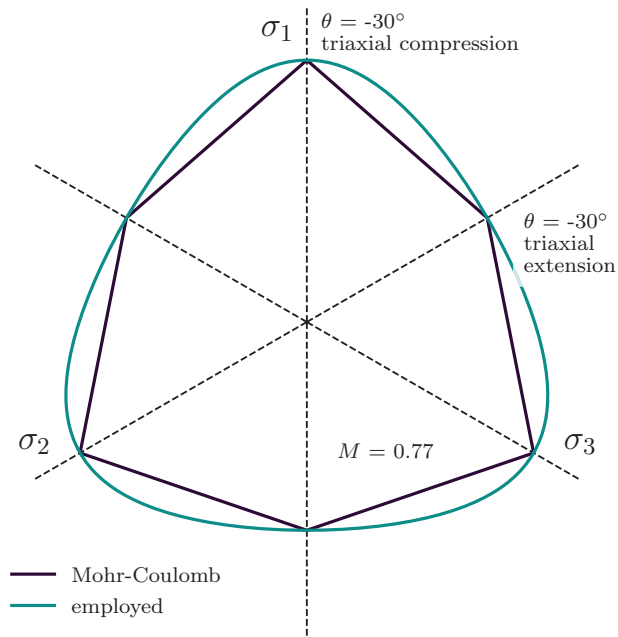


Figure 4: Yield surface adopted in the deviatoric plane.

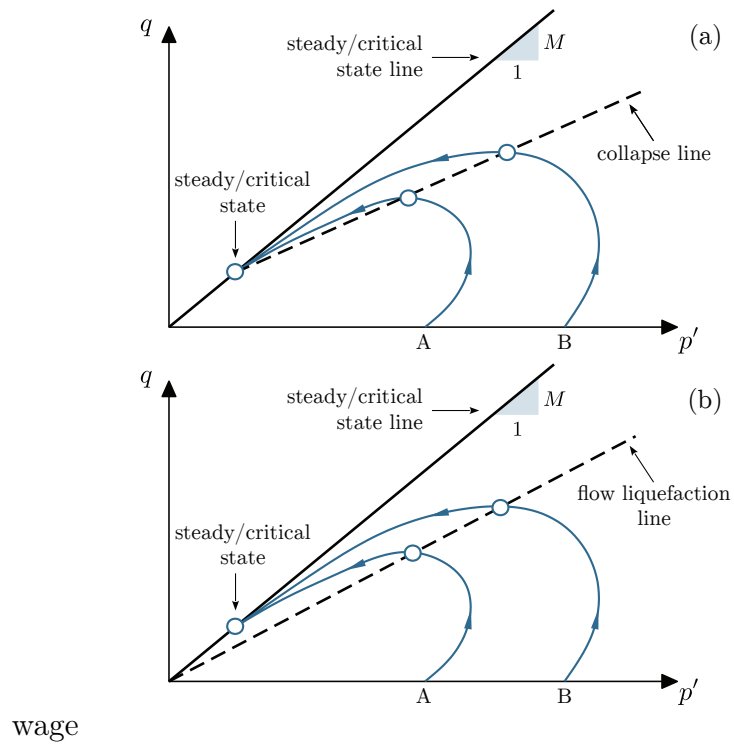


Figure 5: (a) Collapse and (b) flow liquefaction lines concepts (modified from Yang, 2002).

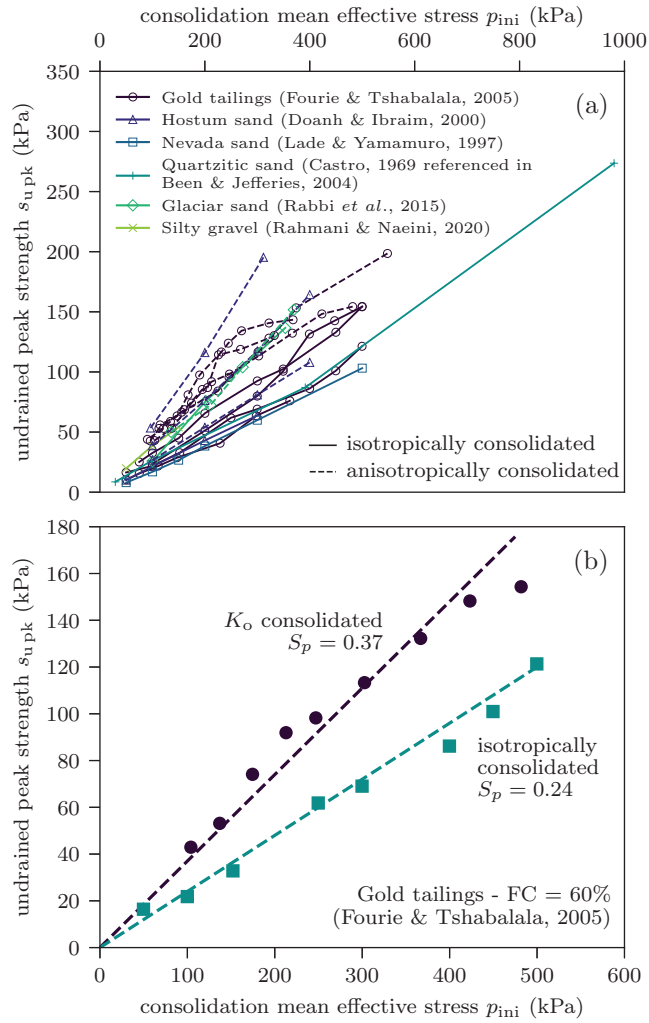


Figure 6: Relationship between the undrained peak strength and the consolidation effective mean stress in triaxial tests on different materials exhibiting flow liquefaction.

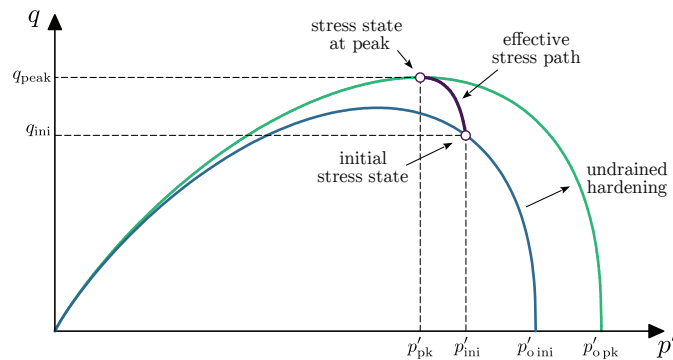


Figure 7: Hardening during undrained loading in CASM.

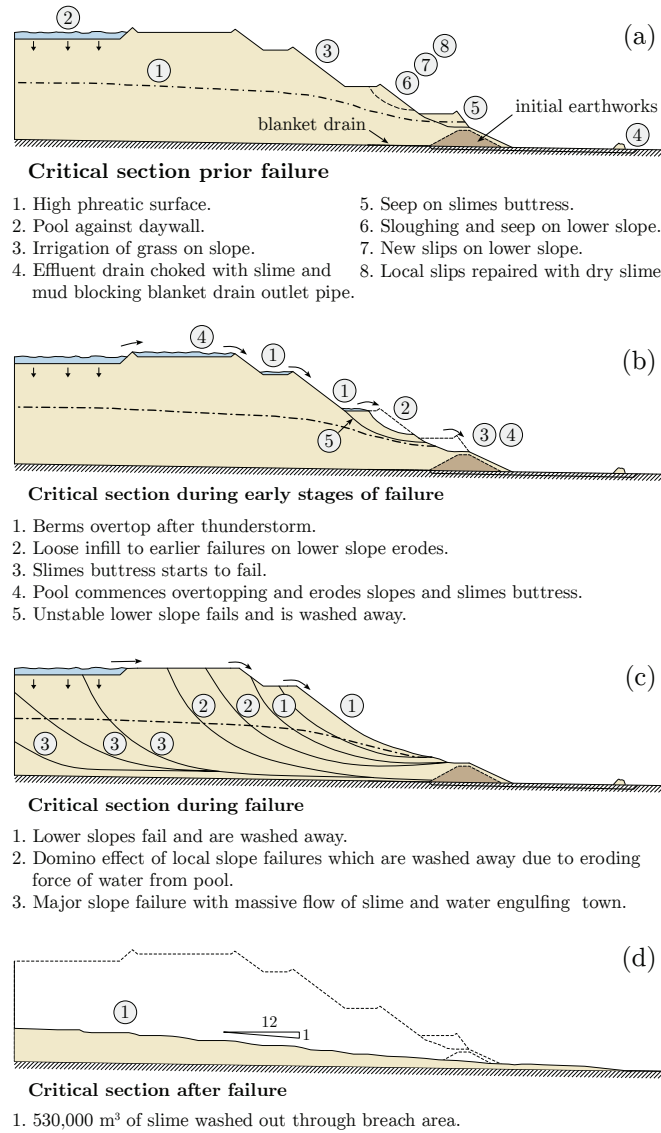


Figure 8: Possible mode of failure of the Merriespruit tailings dam (modified from Wagener, 1997)

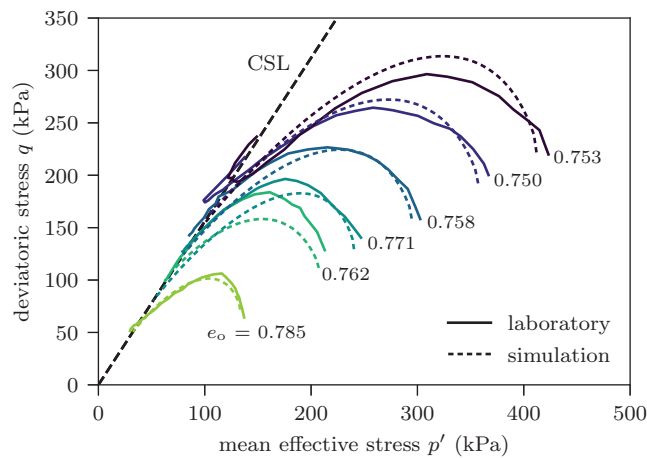


Figure 9: (a) Experimental (Fourie and Tshabalala, 2005) and (b) simulated stress paths for K_o consolidated triaxial tests with $FC=60\%$.

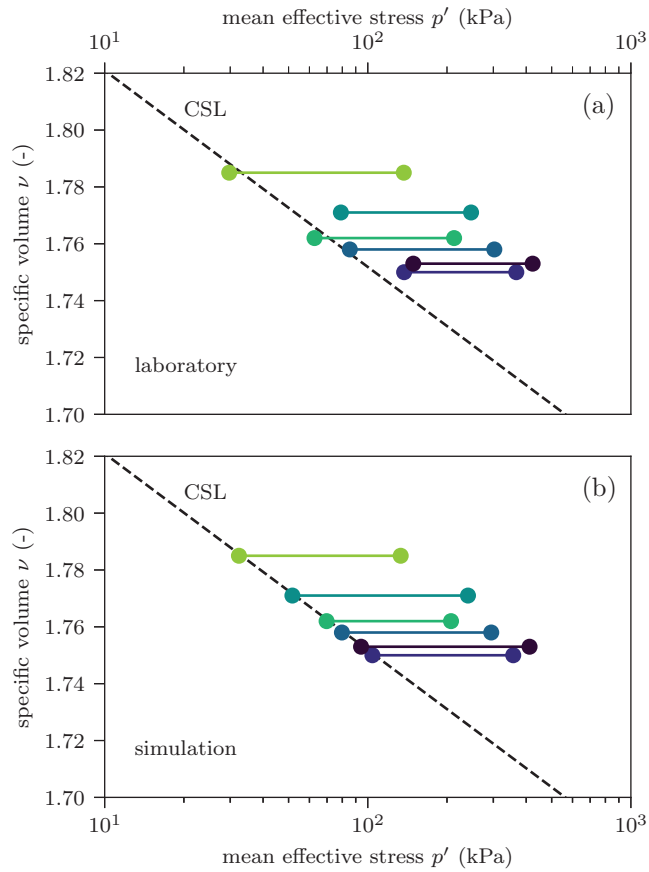


Figure 10: (a) Experimental (Fourie and Tshabalala, 2005) and (b) simulated state diagrams for K_o consolidated triaxial tests with FC=60%.

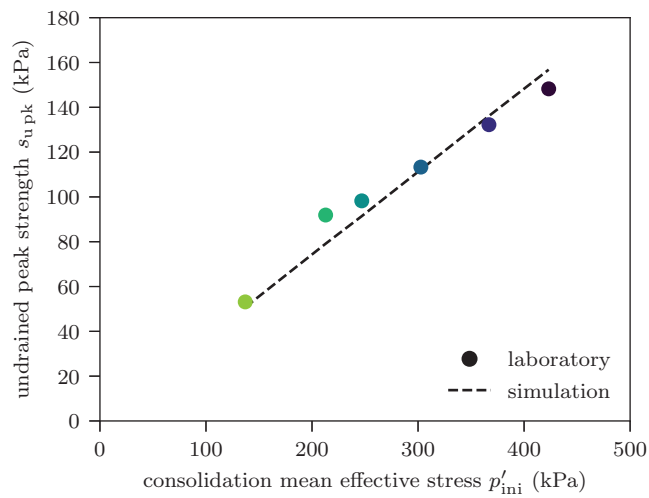


Figure 11: Experimental (Fourie and Tshabalala, 2005) and simulated undrained peak shear strength for K_o consolidated triaxial tests with FC=60%.

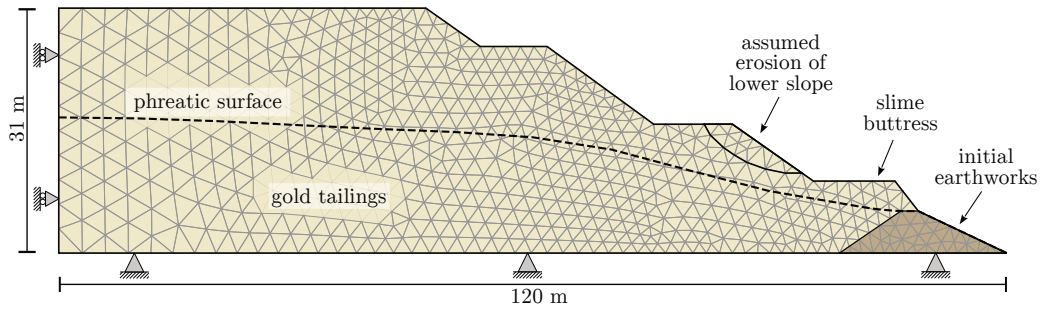


Figure 12: Geometry, boundary conditions, and finite element mesh employed.

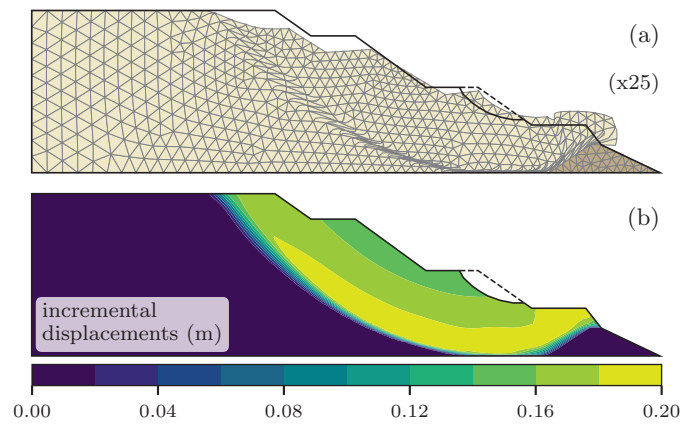


Figure 13: (a) Deformed mesh and (b) incremental displacements at failure

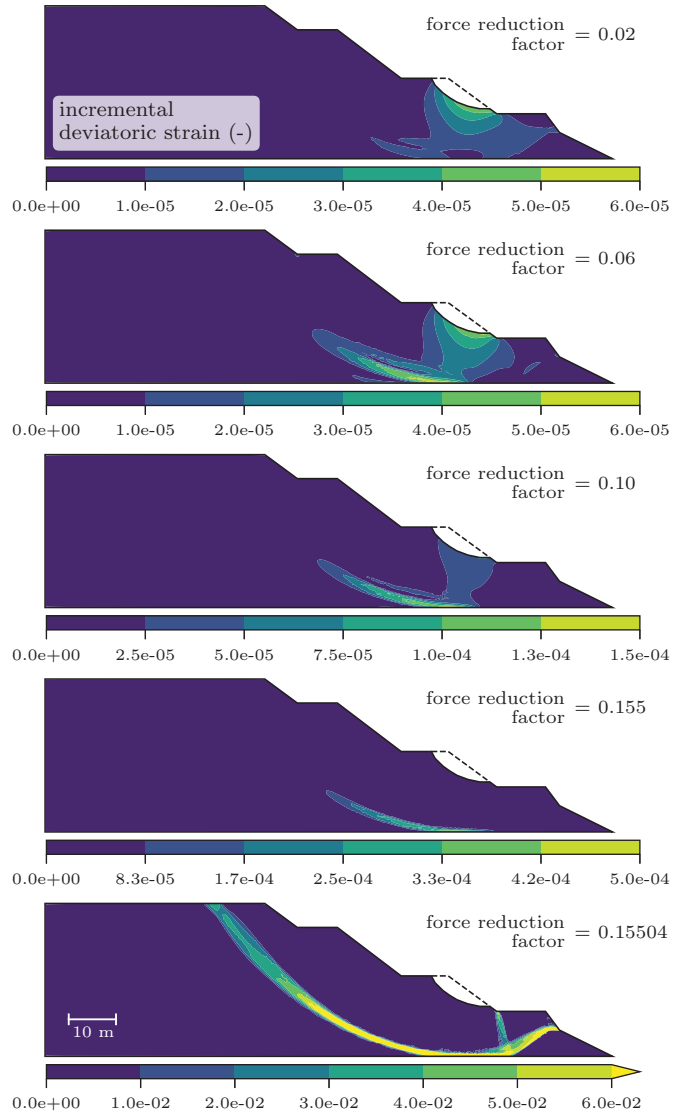


Figure 14: Evolution of the incremental deviatoric strain invariant during the removal of the assumed eroded material.

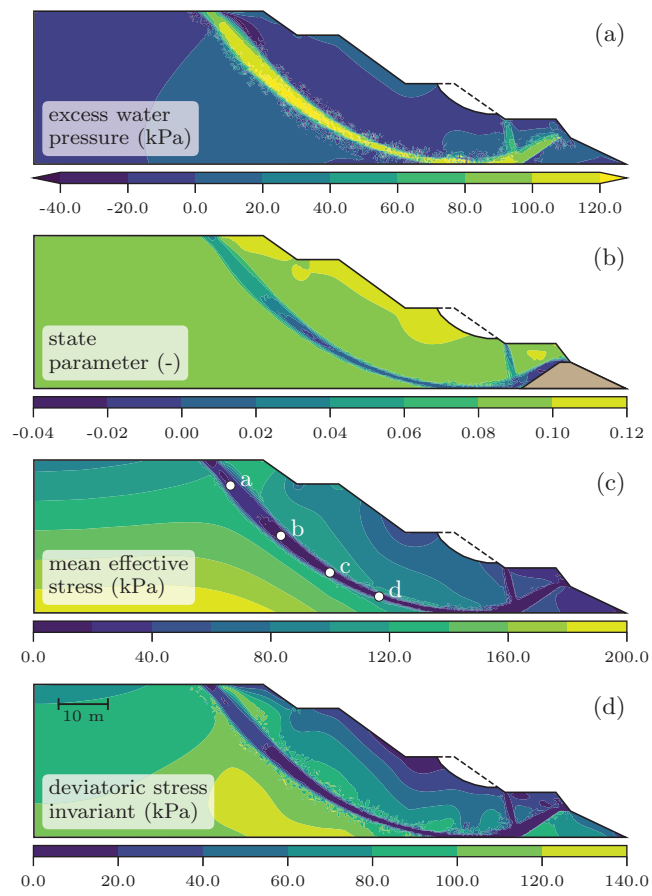


Figure 15: (a) Excess pore-water pressure, (b) state parameter, (c) effective mean stress, and (d) deviatoric stress invariant at failure.

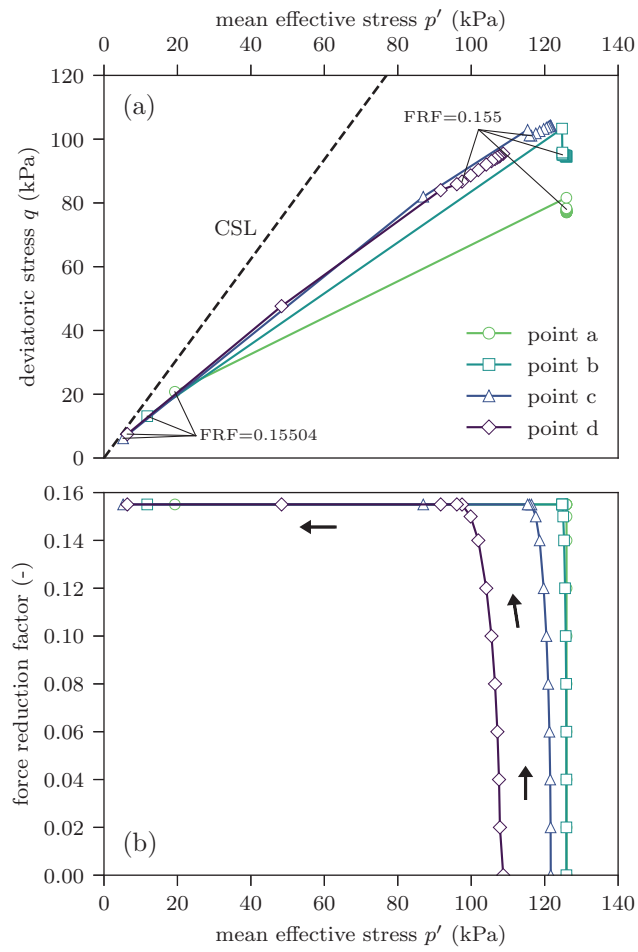


Figure 16: (a) Stress paths and (b) evolution of the force reduction factor for the locations indicated in Figure 15c.

Tables

Table 1: Parameters derived for the K_o consolidated triaxial tests from Fourie and Tshabalala (2005) with FC = 60%.

Parameter	Units	Value
Γ	(-)	1.89
λ	(-)	0.03
κ (assumed)	(-)	0.01
M	(-)	1.56
S_p	(-)	0.37
K_o	(-)	0.60
m	(-)	1.745
ν (assumed)	(-)	0.30

Table 2: Initial state parameters and computed values of n and r for the simulation of the K_o consolidated triaxial tests from Fourie and Tshabalala (2005) with FC = 60%.

Parameter	Units	Value					
		$p'_{ini} = 137$ kPa	213	247	303	367	423
ψ_{ini}	(-)	0.043	0.033	0.046	0.039	0.037	0.044
n	(-)	3.413	2.773	3.601	3.228	3.087	3.509
r	(-)	8.919	5.649	10.643	7.648	6.888	9.740

Table 3: Parameters for the starter dam.

Parameter	Units	Value
Young modulus, E	(kPa)	100e3
Poisson ratio, ν	(-)	0.3
Friction angle, ϕ	(deg)	40
Cohesion, c	(kPa)	20